SCIENTIFIC REPORTS
nature research

Check for updates

OPEN

Enhanced visible light photocatalytic activity of Fe_2O_3 modified TiO_2 prepared by atomic layer deposition

Yan-Qiang Cao[1,2,4], Tao-Qing Zi[1,4], Xi-Rui Zhao[1], Chang Liu[1], Qiang Ren[1], Jia-Bin Fang[1], Wei-Ming Li[1,3] & Ai-Dong Li[1]✉

In this work, commercial anatase TiO_2 powders were modified using ultrathin Fe_2O_3 layer by atomic layer deposition (ALD). The ultrathin Fe_2O_3 coating having small bandgap of 2.20 eV can increase the visible light absorption of TiO_2 supports, at the meantime, Fe_2O_3/TiO_2 heterojunction can effectively improve the lifetime of photogenerated electron–hole pairs. Results of ALD Fe_2O_3 modified TiO_2 catalyst, therefore, showed great visible light driven catalytic degradation of methyl orange compared to pristine TiO_2. A 400 cycles of ALD Fe_2O_3 (~ 2.6 nm) coated TiO_2 powders exhibit the highest degradation efficiency of 97.4% in 90 min, much higher than pristine TiO_2 powders of only 12.5%. Moreover, an ultrathin ALD Al_2O_3 (~ 2 nm) was able to improve the stability of Fe_2O_3-TiO_2 catalyst. These results demonstrate that ALD surface modification with ultrathin coating is an extremely powerful route for the applications in constructing efficient and stable photocatalysts.

A rapid industrial development driven by unsustainable technology advances can cause plenty of industrial sewage, spreading chemical hazards into water resources. As a result, water pollution has emerged as one of the most serious environmental issues worldwide[1–4]. Photocatalytic oxidation technology has shown great prospects in removing the toxic and harmful contaminants in aqueous environment[5–7]. Semiconductors (e.g. TiO_2, ZnO, SnO_2) have been widely researched for organic pollutant degradation, however, the large band gap hinders their practical applications[8–12]. For example, TiO_2 with band gap of 3.2 eV can only absorb the ultra-violet light, accounting for only 4–5% of entire solar spectrum[13]. Therefore, various visible light sensitive photocatalysts has also been widely explored, such as g-C_3N_4, $BiVO_4$, CdSe, Bi_2WO_6[14–19]. On the other hand, TiO_2 is recognized as one of the excellent materials owning to its good inertness, eco-friendly, low cost, strong oxidizing power, and long-term stability against photo and chemical corrosion[9,13,20–22]. Thus, plenty of works have been made to extend the absorption spectrum of TiO_2 to visible light so to make a full use of solar spectrum. Several different approaches can be employed, including doping[23–26] and coupling with small band gap semiconductors or metals[27–30].

Small band gap semiconductors not only increase the absorption of visible light but also inhibit photogenerated electrons-holes recombination when constructed as a semiconductor/semiconductor heterojunction structure, thus improving the photocatalytic performance dramatically[31]. Therefore, various TiO_2 based heterojunction photocatalysts have been proposed for visible light photocatalysis, including NiO/TiO_2[32,33], Ag_2O/TiO_2[34], $CdTe/TiO_2$[35], C_3N_4/TiO_2[36], Bi_2O_3/TiO_2[37], Cu_2O/TiO_2[38], Fe_2O_3/TiO_2[39], etc. For Fe_2O_3/TiO_2 heterojunction photocatalysts, a variety of composites have been investigated, such as Fe_2O_3 nanoparticles on TiO_2 nanotube[40], Fe_2O_3/TiO_2 nanoparticles[41], TiO_2 coated cubic Fe_2O_3[42], Fe_2O_3 nanosheet/TiO_2 hollow sphere[39], and Fe_2O_3 coated TiO_2[43]. For instance, Lin et al. demonstrated that Fe_2O_3 coating can effectively enhance the visible light photocatalytic

[1]National Laboratory of Solid State Microstructures, Jiangsu Key Laboratory of Artificial Functional Materials, Materials Science and Engineering Department, College of Engineering and Applied Sciences, Collaborative Innovation Center of Advanced Microstructures, Jiangsu Key Laboratory of Artificial Functional Materials, Nanjing University, Nanjing 210093, People's Republic of China. [2]Institute of Micro-Nano Photonic and Beam Steering, School of Science, Nanjing University of Science and Technology, Nanjing 210094, People's Republic of China. [3]Jiangsu Leadmicro Nano-Technology Co., Ltd., Wuxi, Jiangsu, People's Republic of China. [4]These authors contributed equally: Yan-Qiang Cao and Tao-Qing Zi. ✉email: adli@nju.edu.cn

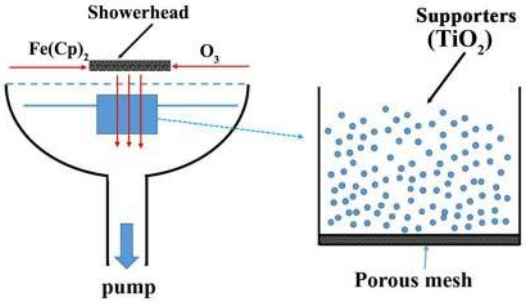

Figure 1. The schematic diagram of coating TiO_2 powders by ALD Fe_2O_3.

activity of TiO_2[43]. Various fabrication methods were applied, including hydrothermal or solvothermal process and sol–gel, to prepare the heterojunction photocatalysts[44–46]. Nevertheless, precise control of the interface between Fe_2O_3 and TiO_2 at atomic level by conventional methods remain challenges.

Atomic layer deposition (ALD) is a unique and promising thin film deposition technique based on self limited and saturated surface chemisorption reactions. It can deposit ultrathin, conformal, and uniform layers at sub-nanometer scale, which has attracted great attentions in surface engineering of nanostructures over the years[47–49]. In catalysts design, ALD enables a conformal layer with precise thickness control and tunable film composition onto another nanostructures with high aspect ratio[50]. The ALD coating can work as photo-active materials[51,52] or surface protection layer[53,54]. Herein, we modified the commercial anatase TiO_2 powders with ultrathin Fe_2O_3 surface coating by ALD. The photocatalytic performance was investigated by visible light degradation of methyl orange (MO). The ultrathin Fe_2O_3 coating can enhance the absorption of TiO_2 supports for visible light. Fe_2O_3 modified TiO_2 powders show much better visible light photocatalytic degradation of MO than pristine TiO_2. A possible mechanism for improved photocatalytic performance is proposed. In addition, an ultrathin ALD Al_2O_3 (~ 2 nm) was used to promote the long-term durability of TiO_2@Fe_2O_3 catalyst.

Methods

ALD deposition on TiO_2 powders. Commercial TiO_2 powders with anatase phase (Nanjing Haitai nano materials Co.) were used as supports in this work. Ferrocene ($Fe(Cp)_2$, Suzhou Fornano Corporation Ltd., 99.99%) and ozone were adopted as Fe and oxygen precursors for ALD Fe_2O_3 deposition. $Fe(Cp)_2$ was vaporized at 85 °C. High purity nitrogen gas (N_2, 99.999%) was used as carrier gas at a total flow rate of 750 sccm and a pressure of 6 hPa in our ALD system (Picosun SUNALE™ R-150B). A particular container with porous mesh was used for ALD coating on powders, which has been reported elsewhere[24,55], as shown in Fig. 1. Herein, precursors can flow through the TiO_2 powders to achieve great conformality. X cycles of ALD Fe_2O_3 (X = 200, 400, 600, and 800) were coated on TiO_2 powder at 300 °C, the samples are marked as TiO_2@X-Fe_2O_3. One cycle of ALD Fe_2O_3 contains the following four steps, 5 s $Fe(Cp)_2$ injection, 20 s N_2 purge, 5 s O_3 injection, and 20 s N_2 purge. At the same system, 20 cycles of Al_2O_3 were deposited on TiO_2@400-Fe_2O_3 at 300 °C, where one ALD cycle of Al_2O_3 is consisted of 5 s trimethylaluminum dose, 20 s N_2 purging, 5 s H_2O dose, and 20 s N_2 purging.

Materials characterizations. X-ray diffraction (XRD) using a Rigaku-D/MAX 2000 system was used for crystallinity and phase structure analysis. Scanning electron microscopy (SEM) images were taken using ZEISS Gemini SEM 500 instrument operated at 2 kV. The high-resolution transmission electron microscopy (HRTEM) was performed on a FEI Tecnai F20 S-Twin to observe the microstructures, where TiO_2 powders were loaded on the ultra-thin carbon coated copper grids. The surface chemical features and valence band spectra were explored by X-ray photoelectron spectroscopy (XPS) using Thermo Fisher K-Alpha. The adventitious carbon signal (C 1 s = 284.6 eV) was adopted to calibrate the binding energies. UV–visible absorption spectra were conducted on a UV–vis-NIR spectrophotometer (UV-3600, Shimadzu, Japan). Photoluminescence (PL) spectra were collected on a Horiba Jobin Yvon HR800 spectrometer.

Photocatalytic degradation. The photocatalytic performance of Fe_2O_3 coated TiO_2 catalysts was investigated by visible light degradation of MO. 100 ml MO solution (4 mg L^{-1}) with 100 mg photocatalysts were loaded into a glass reactor, which was magnetically stirred at 500 rpm. In order to establish the adsorption/desorption equilibrium between MO and catalysts before irradiation, the MO solutions with catalysts were magnetically stirred for 30 min in darkness. Then, the suspension was irradiated under a 300 W Xe lamp (MircoSolar300, Perfect Light). A 420 nm filter was adopted to cut off UV light. The lamp was placed at 15 cm above the suspension, whose average visible light intensity is around 80 mW cm^{-2}. Water cooling was applied throughout the experiment to maintain the temperature at 25 ± 1 °C. 3 mL solution was collected after each 15 min irradiation. The photocatalysts were removed by centrifugal separation. The residual MO concentration was determined using the absorption at 464 nm by UV–Vis–NIR spectrophotometer. The recycled usage experiment was performed for three times to explore the long-term stability of photocatalysts, e.g. after each photocatalytic experiment, the photocatalysts powders were gathered and rinsed by ethanol and water, then baked for 12 h at 100 °C. At last, a new MO solution was used to evaluate the photocatalytic activity of collected photocatalysts.

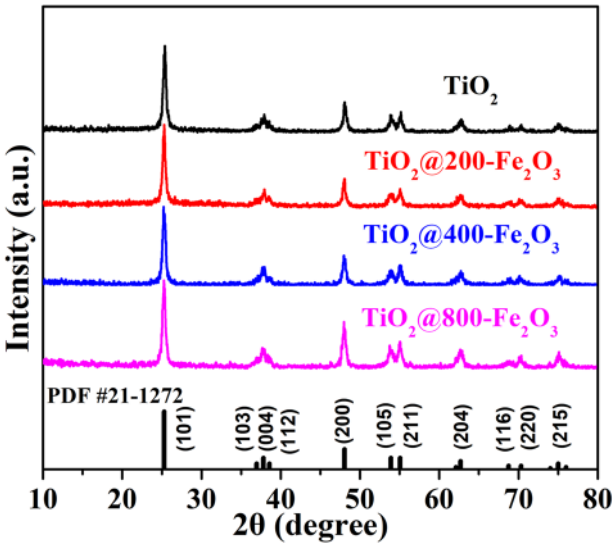

Figure 2. XRD patterns of pristine TiO_2 and Fe_2O_3 coated TiO_2.

Photoelectrochemical measurements. Photoelectrochemical measurements were performed in a three-electrode electrochemical cell at room temperature using 1 M Na_2SO_4 as the electrolyte. The TiO_2 or TiO_2@400-Fe_2O_3 on FTO were used as the working electrode. A Pt wire and Ag/AgCl were used as the counter electrode and the reference electrode, respectively. Photocurrent densities were collected by an electrochemistry workstation (CHI660E, Shanghai) using a potentiostatic method at 0.50 V. Light was chopped on and off cyclically. A solar simulator (300 W Xe lamp, MircoSolar300, Perfect Light) with a 420 nm cut-off filter provides the visible-light irradiation.

Results

Figure 2 depicts the XRD patterns of pristine TiO_2 and Fe_2O_3 coated TiO_2 powders. All the samples show the similar characteristic diffraction peaks, in accord with anatase TiO_2 (JCPDS No. 21–1,272). This result indicates that ultrathin ALD Fe_2O_3 would not affect the crystal structure of TiO_2, consistent with our previous finding[24,55]. In addition, signals related to Fe_2O_3 were absent.

SEM images of TiO_2 powders without and with 400 cycles ALD Fe_2O_3 deposition are shown in Fig. 3a,b. It can be seen that the pristine TiO_2 powder exhibits a disk-like morphology with a diameter of approximately 40 nm and a thickness of approximately 10 nm, with severe aggregation. After ALD Fe_2O_3 deposition, it was observed that Fe_2O_3 coated TiO_2 exhibited almost identical morphology, indicating that ultra-thin Fe_2O_3 coating did not have significant influence on particle size and morphology of TiO_2. HRTEM was further conducted to observe the microstructure of TiO_2@400-Fe_2O_3 and pristine TiO_2 powders as shown in Fig. 3c,d. While pristine TiO_2 shows a sharp well-ordered surface with good crystallinity (Fig. 3c), an amorphous layer of ~ 2.6 nm formed on the TiO_2 surface was observed which was contributed to ultra-thin Fe_2O_3 layer (400 cycles) formed by ALD deposition. Moreover, both samples exhibit the lattice spacing of 0.35 nm, corresponding to (101) planes of anatase TiO_2. Based on above XRD and TEM data, it was speculated that an ultra-thin amorphous Fe_2O_3 is coated on TiO_2 nanoparticles surface without significantly modifying the morphology of the catalyst supports.

To further determine the successful deposition of ALD Fe_2O_3, XPS was performed to characterize the surface chemical features of ALD Fe_2O_3 coated TiO_2 powders. Figure 4a shows the Ti 2p spectra of TiO_2@400-Fe_2O_3 and pristine TiO_2 powders. The spectra can be fitted into two peaks at 464.3 eV and 458.5 eV, which can be assigned to Ti $2p_{1/2}$ and Ti $2p_{3/2}$ peaks[28]. In O 1 s spectra (Fig. 4b), both samples present the main peak at 529.9 eV related to Ti–O bonding from TiO_2. In addition, there is a peak at 531.7 eV can be ascribed to the surface -OH[56]. Figure 4c exhibits the Fe 2p spectrum of TiO_2@400-Fe_2O_3, Fe $2p_{1/2}$ and Fe $2p_{3/2}$ peaks locate at 723.8 eV and 710.5 eV, in accord with Fe–O bonding value in Fe_2O_3[57]. Based on XPS data, the Fe atom ratio (Fe/Fe + Ti) is determined to be 1.1% in TiO_2@400-Fe_2O_3. It is anticipated that an ultra-thin amorphous Fe_2O_3 is coated on TiO_2 nanoparticles surface successfully. Due to the low content of Fe_2O_3, Fe 2p spectrum shows a bad signal to noise ratio. Therefore, the Fe 2p spectrum of ALD Fe_2O_3 film is also presented for reference, as shown in Fig. 4d which can exhibit much better signal to noise ratio.

The influence of ultra-thin Fe_2O_3 coating on absorption of TiO_2 powders in visible light was explored using UV–Vis diffuse reflectance spectra, as illustrated in Fig. 5a. The spectrum of pristine TiO_2 powders is also plotted for comparison. Pristine TiO_2 powders exhibit the absorption edge of around 371 nm without noticeable visible light absorption. However, noticeable absorption in the visible light region from 390 to 750 nm can be observed after ultra-thin Fe_2O_3 surface modification. The relationship of the absorption edge with the photon energy ($h\nu$) for the indirect bandgap semiconductor is shown in the following formula: $(\alpha h\nu)^{1/2} = A(h\nu - E_g)$, where α and A are the absorption coefficient and absorption constant, respectively. Since the absorption coefficient α is determined by the scattering and reflectance spectra based on Kubelka–Munk theory, therefore, the bandgap values

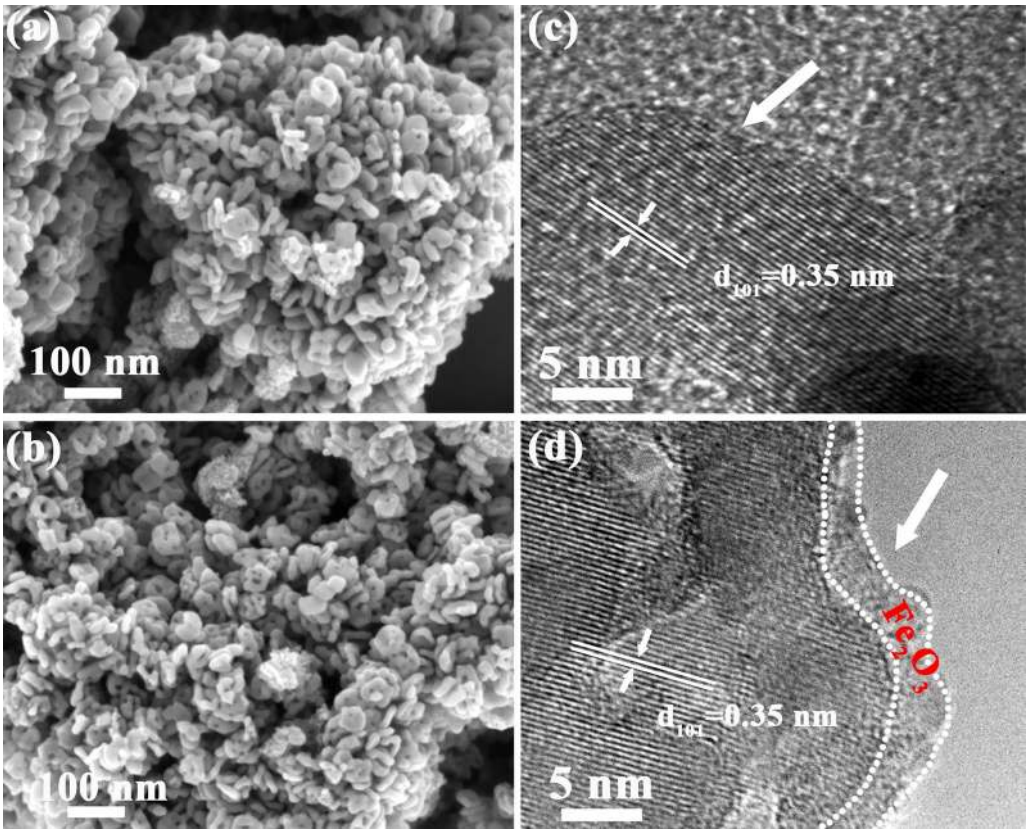

Figure 3. SEM images of (**a**) pristine TiO_2 and (**b**) TiO_2@400-Fe_2O_3. TEM images of (**c**) pristine TiO_2 and (**d**) TiO_2@400-Fe_2O_3.

can be determined by the intercept of the tangent lines. As depicted from Fig. 5b, only one tangent line can be extrapolated for pristine TiO_2 powders showing a bandgap of 3.25 eV, while two bandgap values can be obtained from the plots for TiO_2@400-Fe_2O_3 powders, attributing to Fe_2O_3 coating with a bandgap value of ~ 2.20 eV and TiO_2 supports with a bandgap value of ~ 3.08 eV. It can be concluded that ultra-thin Fe_2O_3 coating results in a smaller bandgap which can increase the absorption of TiO_2 powder support in visible light.

The visible light photocatalytic activity of TiO_2 and Fe_2O_3 coated TiO_2 catalysts was compared by degrading MO. All samples exhibit low adsorption capacity of MO molecules. As reported in our previous work, MO is selected here for its stability under visible light irradiation in the absence of catalysts[24]. Figure 6a shows the evolution of UV–vis absorption spectra of MO solution in the presence of pristine TiO_2 under visible light irradiation. It can been seen that the absorption peaks at 464 nm decreases slightly after 90 min, exhibiting very poor photocatalytic activity due to its large bandgap. In contrast, the peak intensity at 464 nm fades rapidly for TiO_2@400-Fe_2O_3 with the irradiation time extending, as shown in Fig. 6b. In addition, the orange MO solution turns into colorless after 90 min, as presented in the insert of Fig. 6b, indicating the degradation of MO. Figure 6c compares visible light photocatalytic activity of Fe_2O_3 coated TiO_2 catalysts. It can be found that a much-improved photocatalytic degradation efficiency of ~ 86.2% can be achieved with only 200 cycles of ALD Fe_2O_3 modification. And the TiO_2@400-Fe_2O_3 photocatalysts display the highest photocatalytic degradation efficiency of 97.4%. In comparison with reported Fe_2O_3-TiO_2 heterojunction catalysts for photodegradation of organic pollutants and antibiotics, ALD Fe_2O_3 coated TiO_2 (TiO_2@400-Fe_2O_3) in this work exhibit excellent removal efficiency for MO degradation, as summarized in Table 1. The photocatalytic degradation efficiency decreases to 95.8% and 90.4% for TiO_2@600-Fe_2O_3 and TiO_2@800-Fe_2O_3 samples, respectively, along with further increasing the thickness of ALD Fe_2O_3 coating. The reduced efficiency can be ascribed to the fact that more Fe_2O_3 coating would introduce more recombination sites for photoinduced electron–hole pairs[42], diminishing the photocatalytic efficiency.

The degradation data were also fitted by the pseudo-first-order kinetics. The rate constant k can be determined by $\ln(C_t/C_0) = -kt$ at low initial pollutant concentration. Herein, C_0 is the initial MO concentration, while the C_t is the MO concentration after irradiation time of t. k is the first-order rate constant (min^{-1}). The $-\ln(C_t/C_0)$ vs. t curves are plotted in Fig. 6d. It can be seen that $-\ln(C_t/C_0)$ has a linear relationship with t, indicating the photocatalytic degradation of MO by Fe_2O_3 modified TiO_2 catalysts obeys the first-order kinetics. The first-order rate constant (k) is determined to be 3.8×10^{-2} min^{-1} for TiO_2@400-Fe_2O_3, which is much larger than pristine TiO_2 of 1.3×10^{-3} min^{-1}. The result indicates that ALD Fe_2O_3 modification can effectively enhance the visible light photocatalytic performance of TiO_2 supports.

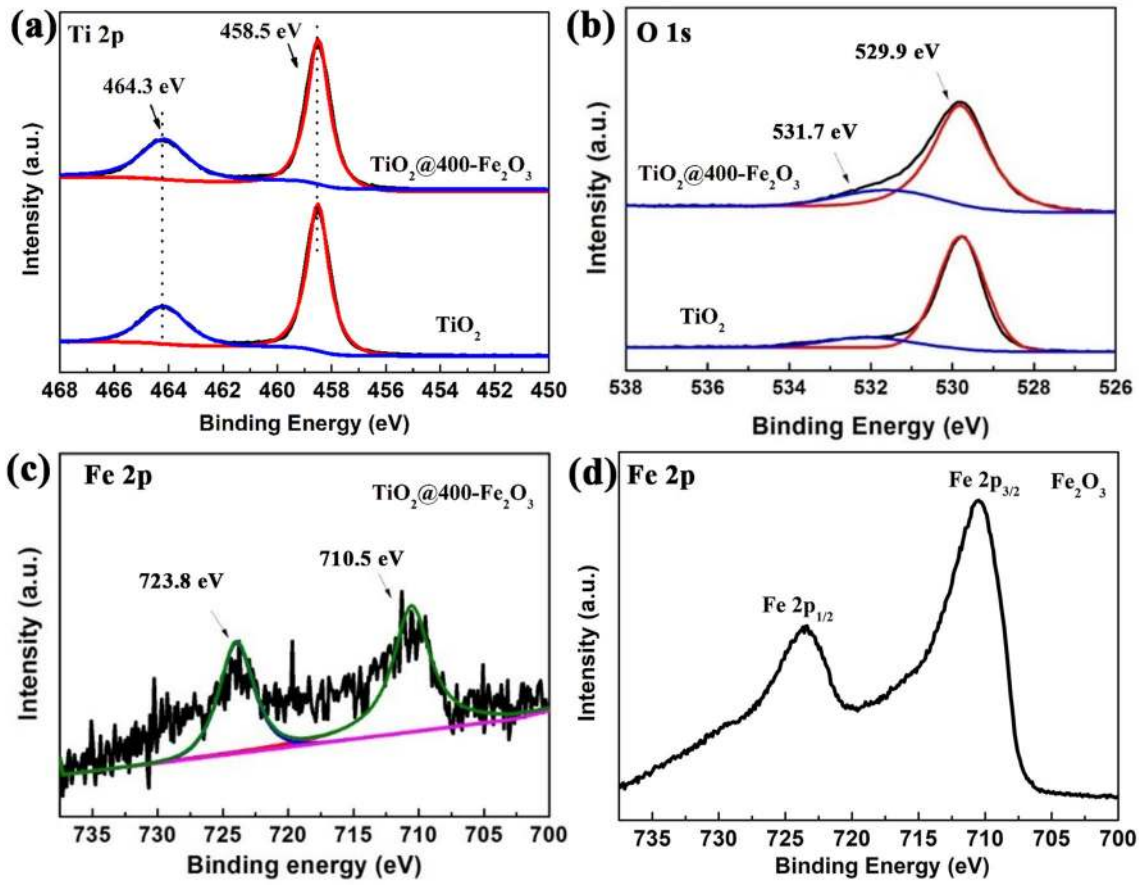

Figure 4. XPS spectra of (**a**) Ti 2p and (**b**) O 1s for TiO_2 and TiO_2@400-Fe_2O_3, Fe 2p XPS spectra for (**c**) TiO_2@400-Fe_2O_3 and (**d**) Fe_2O_3 film.

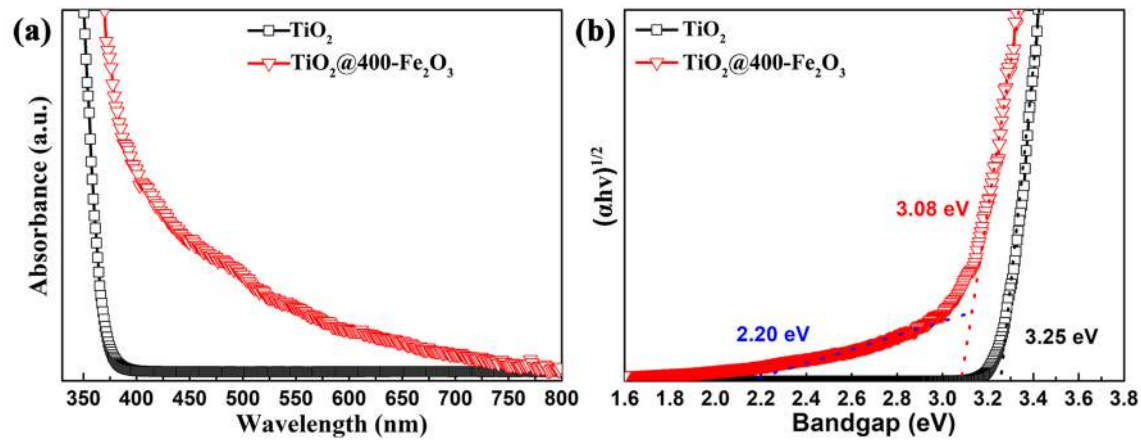

Figure 5. (**a**) UV–Vis diffuse reflectance spectra and (**b**) Tauc plot of TiO_2 with and without 400 cycles Fe_2O_3 coating.

PL and photocurrent response measurements were conducted to explore the recombination rate of photo-generated electron–hole pairs. The lower the PL intensity, the higher separation efficiency of electron–hole pairs in the catalysts. Figure 7a shows the PL spectra of pristine TiO_2 and various cycles of ALD Fe_2O_3 coated TiO_2. It can be seen that all the Fe_2O_3 coated TiO_2 exhibit lower intensity than pristine TiO_2, indicating that the coupling of TiO_2 and Fe_2O_3 can effectively inhibit the recombination of the photo-generated electron–hole pairs. Moreover, it can be seen that the 400 cycles Fe_2O_3 coating results in the lowest intensity, thicker Fe_2O_3 coating would increase the recombination of the photo-generated electron–hole pairs. The PL data are consistent well with the results of photocatalytic degradation of MO. Figure 7b presents the photocurrent response curves of TiO_2 and

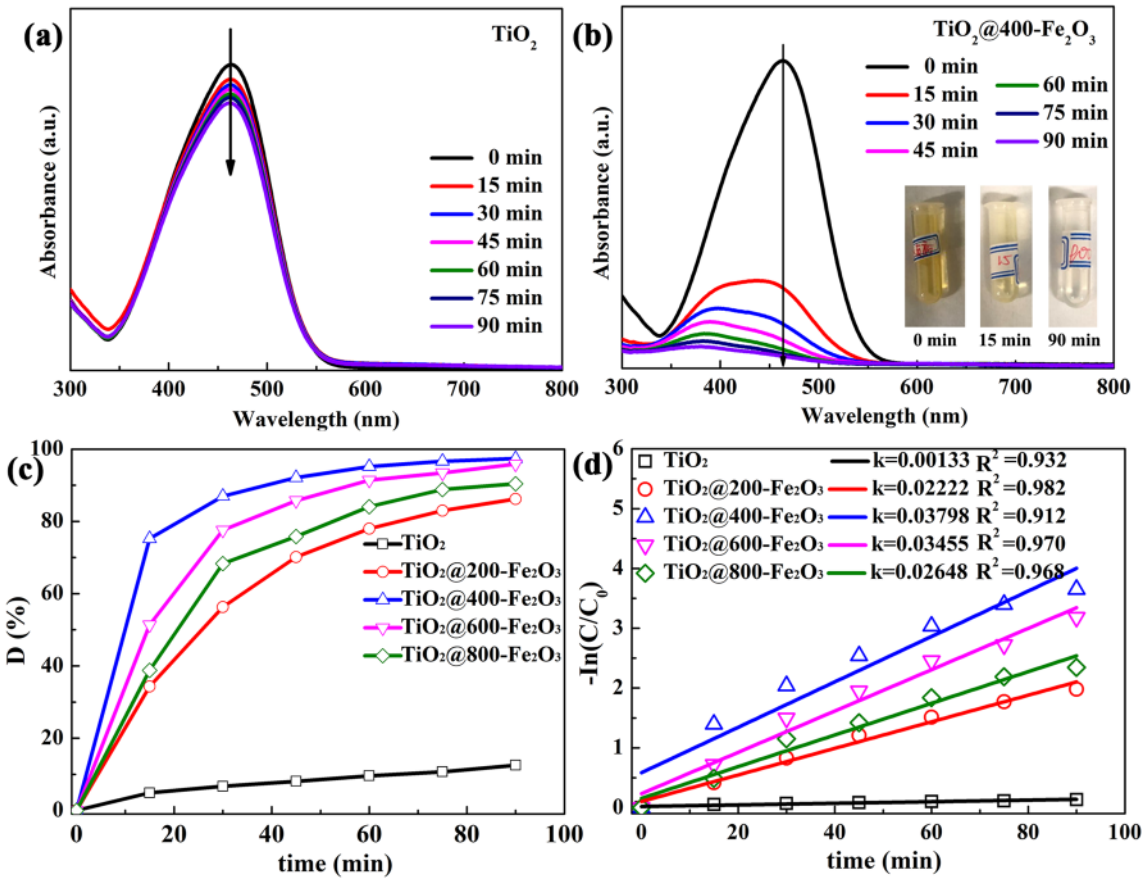

Figure 6. UV–vis absorption spectra of MO exposed to different irradiation time in the presence of (**a**) pristine TiO_2 and (**b**) TiO_2@400-Fe_2O_3 catalysts under visible light irradiation. The inserts are the photos of MO solution before and after irradiation. (**c**) Visible light photocatalytic degradation curves of MO and (**d**) $-\ln(C/C_0)$ vs. time curves by using TiO_2 with and without Fe_2O_3 coating as catalysts.

Catalysts	Method	Power of Xe lamp (W)	Organic pollutants		Time (min)	D (%)	Ref
			type	C (mg L^{-1})			
Fe_2O_3 decorated TiO_2	calcination	350	MB[a]	3.2	80	64.5	58
Fe_2O_3-Doped TiO_2	Sol–gel	500	MB	10	120	100	44
Fe_2O_3/TiO_2 nanofibers	Electrospinning + calcination	800	RhB[b]	5	180	53.6	59
Fe_2O_3 decorated TiO_2	hydrothermal	500	RhB	4.8	270	77.8	45
Fe_2O_3@SiO_2@TiO_2	vapor-thermal	300	RhB	4.8	60	100	46
Fe_2O_3 coated TiO_2	solvothermal	300	TC[c]	50	90	100	39
Core–shell Fe_2O_3@TiO_2	Precipitation	350	RhB	10	360	71.0	60
Core–shell TiO_2@Fe_2O_3	hydrothermal	300	MO	10	16	96.6	43
Core–shell C@TiO_2@Fe_2O_3	Impregnation	500	MB	20	240	80.8	61
Fe_2O_3/TiO_2 composites	Impregnation	500	Orange II	20	240	53.4	62
Fe_2O_3 coated TiO_2	ALD	300	MO	4	90	97.4	This work

Table 1. Comparison of photocatalytic activity for degradation of organic pollutants using TiO_2–Fe_2O_3 based catalysts. [a] MB is Methylene Blue, [b] RhB is Rhodamine B, [c] TC is Tetracycline.

TiO_2@400-Fe_2O_3, it can be seen that TiO_2@400-Fe_2O_3 exhibits a much higher photocurrent density than pristine TiO_2, indicating a more efficient separation of the photoexcited electron–hole pairs.

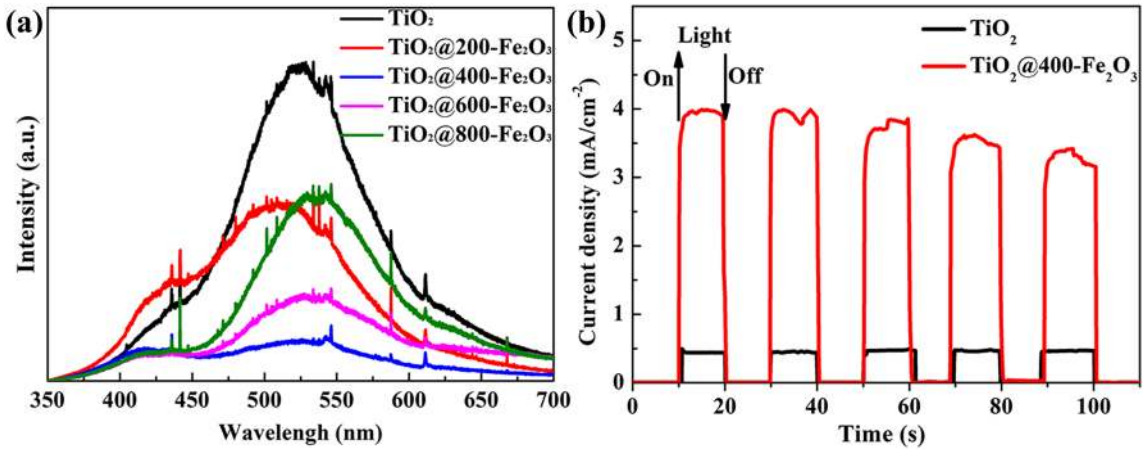

Figure 7. (**a**) PL spectra and (**b**) photocurrent response curves of TiO_2 and Fe_2O_3 coated TiO_2.

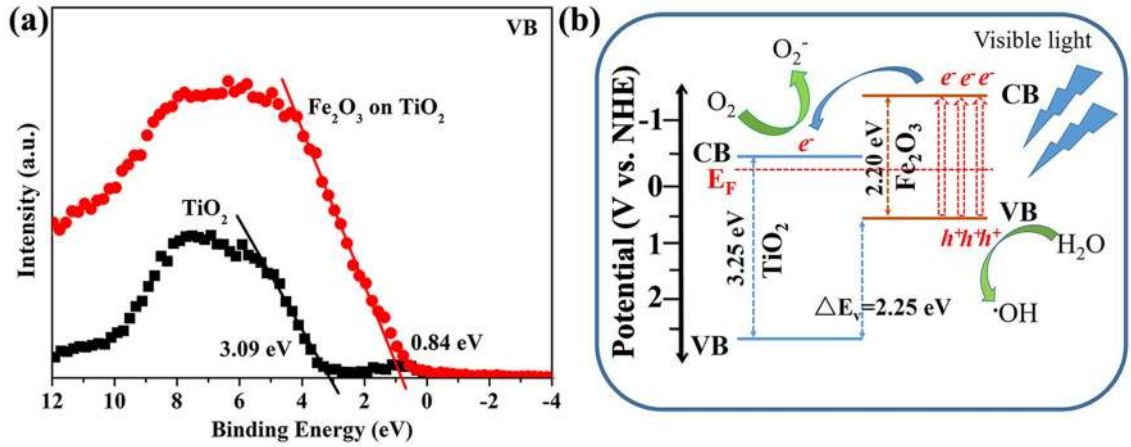

Figure 8. (**a**) Valence band spectra of TiO_2 and Fe_2O_3–TiO_2. (**b**) Schematic illustration of energy band structure of Fe_2O_3 coated TiO_2 and proposed charge transfer mechanism during visible light irradiation.

The band alignment for Fe_2O_3 coated TiO_2 was determined by measuring the valence band offset ΔE_v (VBO) using XPS. Figure 8a shows VB spectra of TiO_2 and Fe_2O_3–TiO_2 determined by linear extrapolation method, respectively. The VB of TiO_2 and Fe_2O_3–TiO_2 are found to be 3.09 eV and 0.84 eV, respectively. The VB of Fe_2O_3 is higher than that of TiO_2, and ΔE_v at the interface of Fe_2O_3-TiO_2 is estimated to be 2.25 eV. The optical bandgaps of TiO_2 and Fe_2O_3 have been determined to be 3.25 and 2.20 eV, respectively, in Fig. 5. Therefore, the conduction band offset ΔE_c (CBO) at the interface of Fe_2O_3-TiO_2 is estimated to be 1.20 eV. Considering the band structure of TiO_2 vs. standard hydrogen electrode (NHE)[62–64], the energy band structure of Fe_2O_3 coated TiO_2 can be depicted in Fig. 8b. Under visible light, TiO_2 shows no photo-electronic response due to its large band gap. Only Fe_2O_3 can be excited, yielding photo-generated electron from its VB to CB. Due to the aligned equilibrium of Fermi level at the interface of TiO_2 and Fe_2O_3, as shown in Fig. 8b, the photogenerated electrons can transfer from CB of Fe_2O_3 to that of TiO_2 driven by the built-in electric field and the concentration gradient of electrons, while remaining the holes in VB of Fe_2O_3[60,62–64]. Therefore, the separation efficiency of photoinduced electron–hole pairs can be improved, which has been demonstrated by PL and photocurrent response results in Fig. 7. There are a large number of literatures focusing on the photocatalytic activity of Fe_2O_3-TiO_2 composites catalyst[60,62–64]. It is widely accepted that OH· radicals can be formed via the reaction of water and photogenerated holes in VB of Fe_2O_3. And electrons in CB of TiO_2 can react with oxygen to form O_2^-. These radicals with high activities can degrade organic molecules into harmless substances.

The stability of photocatalysts is one of the significant factors for practical applications, therefore, TiO_2@400-Fe_2O_3 and TiO_2@800-Fe_2O_3 catalysts were tested in recycling experiments of MO photodegradation. As shown in Fig. 9a, compared to the first usage, both TiO_2@400-Fe_2O_3 and TiO_2@800-Fe_2O_3 catalysts exhibit a declining degradation efficiency. The degradation efficiency retention compared to the first usage is only 59.6% and 66.7% for TiO_2@400-Fe_2O_3 and TiO_2@800-Fe_2O_3, respectively. It may be ascribed to the fact that stability of Fe_2O_3 during photocatalytic reactions is reduced due to photo-corrosion[42,65]. ALD coatings have been widely used as surface protection layer to protect active materials from photo-corrosion[53,54]. Therefore, an ultrathin Al_2O_3 (~2 nm) protective layer was deposited on catalysts surface by ALD in the same system to

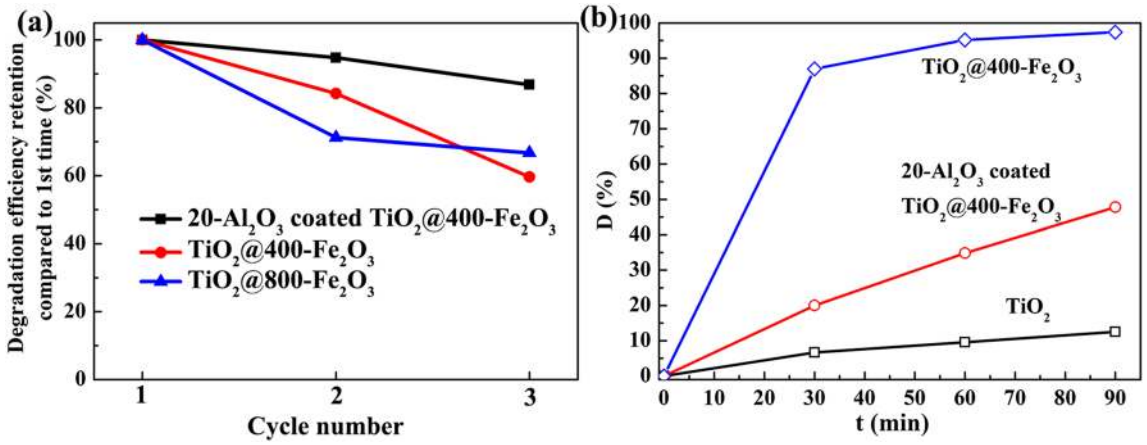

Figure 9. (**a**) Three cycles of MO degradation for TiO_2@400-Fe_2O_3, TiO_2@800-Fe_2O_3 and 20 cycles Al_2O_3 coated TiO_2@400-Fe_2O_3 in 90 min. (**b**) Comparison of MO degradation curves for pristine TiO_2, TiO_2@400-Fe_2O_3, and 20 cycles Al_2O_3 coated TiO_2@400-Fe_2O_3.

improve the stability of Fe_2O_3 coated TiO_2 catalysts. Figure 9b shows the photocatalytic degradation of MO using both TiO_2@400-Fe_2O_3 with Al_2O_3 passivation. The photocatalytic degradation efficiency decreases to 47.8% in 90 min, which is ascribed to the fact that Al_2O_3 coating with large band gap would also hinder the photogenerated carriers form migrating to the surface of electrode[62,66]. But it is still much better than that of pristine TiO_2. More importantly, the stability of catalysts is persistent, as there is limited decline of degradation efficiency after three usage as shown in Fig. 8a, retaining 86.8% compared to the first usage. The results indicate that thin Al_2O_3 can act as a physical shell to protect Fe_2O_3 from photo-corrosion. This can be ascribed to that Al_2O_3 can prevent the direct contact between solution and Fe_2O_3.

Conclusions. In summary, commercial anatase TiO_2 powders were modified using ultrathin ALD Fe_2O_3 surface coating. The ultrathin Fe_2O_3 layer with small bandgap of ~ 2.20 V can increase the absorption of TiO_2 supports in visible light. In addition, Fe_2O_3/TiO_2 heterojunction can suppress the photoinduced electron–hole pairs recombination. The above results indicate excellent visible light photocatalytic activity for the Fe_2O_3 modified TiO_2 powders. 400 cycles Fe_2O_3 (~ 2.6 nm) coated TiO_2 photocatalysts show excellent degradation efficiency of 97.4% in 90 min, far above the performance of pristine TiO_2 powders with only 12.5%. Moreover, an ultrathin Al_2O_3 (~ 2 nm) can improve the recycling usage performance of Fe_2O_3 coated TiO_2 catalyst effectively. As conclusions, ALD surface modification with ultrathin film is a promising route for improving the visible light activity and long-term stability of photocatalysts.

Received: 16 January 2020; Accepted: 28 July 2020
Published online: 10 August 2020

References

1. Schultz, D. M. & Yoon, T. P. Solar synthesis: prospects in visible light photocatalysis. *Science* **343**, 1239176 (2014).
2. Yu, C., Li, G., Kumar, S., Yang, K. & Jin, R. Phase transformation synthesis of novel Ag_2O/Ag_2CO_3 heterostructures with high visible light efficiency in photocatalytic degradation of pollutants. *Adv. Mater.* **26**, 892–898 (2014).
3. Dong, W. *et al.* Preparation of secondary mesopores in mesoporous anatase-silica nanocomposites with unprecedented-high photocatalytic degradation performances. *Adv. Funct. Mater.* **26**, 964–976 (2016).
4. Asahi, R., Morikawa, T., Ohwaki, T., Aoki, K. & Taga, Y. Visible-light photocatalysis in nitrogen-doped titanium oxides. *Science* **293**, 269–271 (2001).
5. Mills, A., Davies, R. H. & Worsley, D. Water purification by semiconductor photocatalysis. *Chem. Soc. Rev.* **22**, 417–425 (1993).
6. Malato, S., Fernández-Ibáñez, P., Maldonado, M. I., Blanco, J. & Gernjak, W. Decontamination and disinfection of water by solar photocatalysis: recent overview and trends. *Catal. Today* **147**, 1–59 (2009).
7. Byrne, C., Subramanian, G. & Pillai, S. C. Recent advances in photocatalysis for environmental applications. *J. Environ. Chem. Eng.* **6**, 3531–3555 (2018).
8. Cao, Y. Q. *et al.* Photocatalytic activity and photocorrosion of atomic layer deposited ZnO ultrathin films for the degradation of methylene blue. *Nanotechnology* **26**, 024002 (2015).
9. Xing, Z. *et al.* Recent advances in floating TiO_2-based photocatalysts for environmental application. *Appl. Catal. B* **225**, 452–467 (2018).
10. Parale, V. G., Kim, T., Phadtare, V. D., Yadav, H. M. & Park, H.-H. Enhanced photocatalytic activity of a mesoporous TiO_2 aerogel decorated onto three-dimensional carbon foam. *J. Mol. Liq.* **277**, 424–433 (2019).
11. Kim, T. *et al.* Facile synthesis of SnO_2 aerogel/reduced graphene oxide nanocomposites via in situ annealing for the photocatalytic degradation of methyl orange. *Nanomaterials* **9**, 358 (2019).
12. Parale, V. G. *et al.* SnO_2 aerogel deposited onto polymer-derived carbon foam for environmental remediation. *J. Mol. Liq.* **287**, 110990 (2019).
13. Linsebigler, A. L., Lu, G. & Yates, J. T. Jr. Photocatalysis on TiO_2 surfaces: principles, mechanisms, and selected results. *Chem. Rev.* **95**, 735–758 (1995).
14. Paul, D. R. *et al.* Synthesis, characterization and application of silver doped graphitic carbon nitride as photocatalyst towards visible light photocatalytic hydrogen evolution. *Int. J. Hydrogen Energy* https://doi.org/10.1016/j.ijhydene.2019.06.061 (2019).

15. Paul, D. R., Sharma, R., Nehra, S. P. & Sharma, A. Effect of calcination temperature, pH and catalyst loading on photodegradation efficiency of urea derived graphitic carbon nitride towards methylene blue dye solution. *RSC Adv.* **9**, 15381–15391 (2019).
16. Devina, *et al.* Silver doped graphitic carbon nitride for the enhanced photocatalytic activity towards organic dyes. *J. Nanosci. Nanotechnol.* **19**, 5241–5248 (2019).
17. Patidar, D., Yadav, A., Paul, D. R., Sharma, A. & Nehra, S. P. Nanohybrids cadmium selenide-reduced graphene oxide for improving photo-degradation of methylene blue. *Physica E* **114**, 113560 (2019).
18. Fu, H., Pan, C., Yao, W. & Zhu, Y. Visible-light-induced degradation of rhodamine B by nanosized Bi_2WO_6. *J. Phys. Chem. B* **109**, 22432–22439 (2005).
19. Lin, X. *et al.* Graphitic carbon nitride quantum dots and nitrogen-doped carbon quantum dots co-decorated with $BiVO_4$ microspheres: a ternary heterostructure photocatalyst for water purification. *Sep. Purif. Technol.* **226**, 117–127 (2019).
20. Fujishima, A., Rao, T. N. & Tryk, D. A. Titanium dioxide photocatalysis. *J. Photochem. Photobiol., C* **1**, 1–21 (2000).
21. Nakata, K. & Fujishima, A. TiO2 photocatalysis: design and applications. *J. Photochem. Photobiol., C* **13**, 169–189 (2012).
22. Qian, R. *et al.* Charge carrier trapping, recombination and transfer during TiO_2 photocatalysis: an overview. *Catal. Today* **335**, 78–90 (2019).
23. Zhou, F., Yan, C., Sun, Q. & Komarneni, S. TiO_2/Sepiolite nanocomposites doped with rare earth ions: Preparation, characterization and visible light photocatalytic activity. *Microporous Mesoporous Mater.* **274**, 25–32 (2019).
24. Cao, Y.-Q. *et al.* TiO_xN_y modified TiO_2 powders prepared by plasma enhanced atomic layer deposition for highly visible light photocatalysis. *Sci. Reports* **8**, 12131 (2018).
25. Song, J. *et al.* Photocatalytic enhancement of floating photocatalyst: layer-by-layer hybrid carbonized chitosan and Fe–N–codoped TiO_2 on fly ash cenospheres. *Appl. Surf. Sci.* **391**, 236–250 (2017).
26. Lee, H., Kim, B.-J., Park, Y.-K., Kim, J.-S. & Jung, S.-C. Assessment of photocatalytic performance of Fe/N-TiO_2 photocatalysts prepared by liquid phase plasma process. *Catal. Today* https://doi.org/10.1016/j.cattod.2019.07.008 (2019).
27. Choi, T., Kim, J.-S. & Kim, J. H. Transparent nitrogen doped TiO_2/WO_3 composite films for self-cleaning glass applications with improved photodegradation activity. *Adv. Powder Technol.* **27**, 347–353 (2016).
28. Guo, X. *et al.* Porous TiB_2-TiC/TiO_2 heterostructures: Synthesis and enhanced photocatalytic properties from nanosheets to sweetened rolls. *Appl. Catal. B* **217**, 12–20 (2017).
29. Zhao, H. *et al.* Synthesis of hierarchically meso-macroporous TiO_2/CdS heterojunction photocatalysts with excellent visible-light photocatalytic activity. *J. Colloid Interface Sci.* **512**, 47–54 (2018).
30. Cao, Y. *et al.* Mesoporous black TiO_{2-x}/Ag nanospheres coupled with g-C_3N_4 nanosheets as 3D/2D ternary heterojunctions visible light photocatalysts. *J. Hazard. Mater.* **343**, 181–190 (2018).
31. Hou, J., Cheng, H., Yang, C., Takeda, O. & Zhu, H. Hierarchical carbon quantum dots/hydrogenated-γ-TaON heterojunctions for broad spectrum photocatalytic performance. *Nano Energy* **18**, 143–153 (2015).
32. Wang, M. *et al.* TiO_2/NiO hybrid shells: p–n junction photocatalysts with enhanced activity under visible light. *J. Mater. Chem. A* **3**, 20727–20735 (2015).
33. Liu, J. *et al.* Black NiO–TiO_2 nanorods for solar photocatalysis: recognition of electronic structure and reaction mechanism. *Appl. Catal. B* **224**, 705–714 (2018).
34. Zhou, W. *et al.* Ag_2O/TiO_2 nanobelts heterostructure with enhanced ultraviolet and visible photocatalytic activity. *ACS Appl. Mater. Interfaces.* **2**, 2385–2392 (2010).
35. Gong, Y. *et al.* All-solid-state Z-scheme CdTe/TiO_2 heterostructure photocatalysts with enhanced visible-light photocatalytic degradation of antibiotic waste water. *Chem. Eng. J.* **350**, 257–267 (2018).
36. Hao, R., Wang, G., Jiang, C., Tang, H. & Xu, Q. In situ hydrothermal synthesis of g-C_3N_4/TiO_2 heterojunction photocatalysts with high specific surface area for Rhodamine B degradation. *Appl. Surf. Sci.* **411**, 400–410 (2017).
37. Sood, S., Mehta, S. K., Sinha, A. S. K. & Kansal, S. K. Bi_2O_3/TiO_2 heterostructures: synthesis, characterization and their application in solar light mediated photocatalyzed degradation of an antibiotic, ofloxacin. *Chem. Eng. J.* **290**, 45–52 (2016).
38. Yang, L. *et al.* High efficient photocatalytic degradation of p-nitrophenol on a unique Cu_2O/TiO_2 p–n heterojunction network catalyst. *Environ. Sci. Technol.* **44**, 7641–7646 (2010).
39. Ren, L. *et al.* Defects-engineering of magnetic γ-Fe_2O_3 ultrathin nanosheets/mesoporous black TiO_2 hollow sphere heterojunctions for efficient charge separation and the solar-driven photocatalytic mechanism of tetracycline degradation. *Appl. Catal. B* **240**, 319–328 (2019).
40. Xu, Z. *et al.* Sulfate functionalized Fe_2O_3 nanoparticles on TiO_2 nanotube as efficient visible light-active photo-fenton catalyst. *Ind. Eng. Chem. Res.* **54**, 4593–4602 (2015).
41. Hassan, M. E., Chen, Y., Liu, G., Zhu, D. & Cai, J. Heterogeneous photo-Fenton degradation of methyl orange by Fe_2O_3/TiO_2 nanoparticles under visible light. *J. Water Process Eng.* **12**, 52–57 (2016).
42. Zheng, X., Fu, W., Kang, F., Peng, H. & Wen, J. Enhanced photo-Fenton degradation of tetracycline using TiO_2-coated α-Fe_2O_3 core–shell heterojunction. *J. Ind. Eng. Chem.* **68**, 14–23 (2018).
43. Lin, Z., Liu, P., Yan, J. & Yang, G. Matching energy levels between TiO_2 and α-Fe_2O_3 in a core–shell nanoparticle for visible-light photocatalysis. *J. Mater. Chem. A* **3**, 14853–14863 (2015).
44. Cao, X., Luo, S., Liu, C. & Chen, J. Synthesis of bentonite-supported Fe_2O_3-doped TiO_2 superstructures for highly promoted photocatalytic activity and recyclability. *Adv. Powder Technol.* **28**, 993–999 (2017).
45. Cheng, G. *et al.* A novel protocol to design TiO_2–Fe_2O_3 hybrids with effective charge separation efficiency for improved photocatalysis. *Adv. Powder Technol.* **28**, 665–670 (2017).
46. Yu, X., Liu, S. & Yu, J. Superparamagnetic γ-Fe_2O_3@SiO_2@TiO_2 composite microspheres with superior photocatalytic properties. *Appl. Catal. B* **104**, 12–20 (2011).
47. Liu, M., Li, X., Karuturi, S. K., Tok, A. I. Y. & Fan, H. J. Atomic layer deposition for nanofabrication and interface engineering. *Nanoscale* **4**, 1522–1528 (2012).
48. Knez, M., Nielsch, K. & Niinistö, L. Synthesis and surface engineering of complex nanostructures by atomic layer deposition. *Adv. Mater.* **19**, 3425–3438 (2007).
49. Meng, X. *et al.* Atomic layer deposition for nanomaterials synthesis and functionalization in energy technology. *Mater. Horizons* **4**, 133–154 (2017).
50. O'Neill, B. J. *et al.* Catalyst design with atomic layer deposition. *ACS Catal.* **5**, 1804–1825 (2015).
51. Liu, J. *et al.* Enhanced photochemical catalysis of TiO_2 inverse opals by modification with ZnO or Fe_2O_3 using ALD and the hydrothermal method. *Mater. Res. Express* **5**, 025509 (2018).
52. Hiltunen, A. *et al.* Design aspects of all atomic layer deposited TiO_2–Fe_2O_3 scaffold-absorber photoanodes for water splitting. *Sustain. Energy Fuels* **2**, 2124–2130 (2018).
53. Long, J. *et al.* High-quality ZnO inverse opals and related heterostructures as photocatalysts produced by atomic layer deposition. *Appl. Surf. Sci.* **454**, 112–120 (2018).
54. Cheng, Q. *et al.* Al_2O_3 and SiO_2 atomic layer deposition layers on ZnO photoanodes and degradation mechanisms. *ACS Appl. Mater. Interfaces.* **9**, 16138–16147 (2017).
55. Zhao, X.-R. *et al.* Photocatalytic properties of Co_3O_4-coated TiO_2 powders prepared by plasma-enhanced atomic layer deposition. *Nanoscale Res. Lett.* **12**, 497 (2017).

56. Yan, X. *et al.* The interplay of sulfur doping and surface hydroxyl in band gap engineering: mesoporous sulfur-doped TiO_2 coupled with magnetite as a recyclable, efficient, visible light active photocatalyst for water purification. *Appl. Catal. B* **218**, 20–31 (2017).
57. Nefedov, V. I., Salyn, Y. V., Leonhardt, G. & Scheibe, R. A comparison of different spectrometers and charge corrections used in X-ray photoelectron spectroscopy. *J. Electron Spectrosc. Relat. Phenom.* **10**, 121–124 (1977).
58. Cheng, L., Qiu, S., Chen, J., Shao, J. & Cao, S. A practical pathway for the preparation of Fe_2O_3 decorated TiO_2 photocatalyst with enhanced visible-light photoactivity. *Mater. Chem. Phys.* **190**, 53–61 (2017).
59. Liu, H. *et al.* Highly flexible Fe_2O_3/TiO_2 composite nanofibers for photocatalysis and utraviolet detection. *J. Phys. Chem. Solids* **121**, 236–246 (2018).
60. Zhang, X. *et al.* One-dimensional mesoporous $Fe_2O_3@TiO_2$ core–shell nanocomposites: rational design, synthesis and application as high-performance photocatalyst in visible and UV light region. *Appl. Surf. Sci.* **317**, 43–48 (2014).
61. Li, J., Liu, Z., Wang, D. & Zhu, Z. Visible-light responsive carbon–anatase–hematite core–shell microspheres for methylene blue photodegradation. *Mater. Sci. Semicond. Process.* **27**, 950–957 (2014).
62. Peng, L., Xie, T., Lu, Y., Fan, H. & Wang, D. Synthesis, photoelectric properties and photocatalytic activity of the Fe_2O_3/TiO_2 heterogeneous photocatalysts. *Phys. Chem. Chem. Phys.* **12**, 8033 (2010).
63. Sun, B. *et al.* Magnetic Fe_2O_3/mesoporous black TiO_2 hollow sphere heterojunctions with wide-spectrum response and magnetic separation. *Appl. Catal. B* **221**, 235–242 (2018).
64. Liu, J. *et al.* 3D flower-like α-$Fe_2O_3@TiO_2$ core–shell nanostructures: general synthesis and enhanced photocatalytic performances. *ACS Sustain. Chem. Eng.* **3**, 2975–2984 (2015).
65. Krýsa, J. *et al.* α-Fe_2O_3/TiO_2 stratified photoanodes. *J. Photochem. Photobiol., A* **366**, 12–17 (2018).
66. Jiao, W. *et al.* Hollow hematite single crystals deposited with ultra-thin Al_2O_3 by atom layer deposition for improved photoelectrochemical performance. *Dalton Trans.* **46**, 10635–10640 (2017).

Acknowledgements

This work is supported by Natural Science Foundation of China (51802150, 51721001, and 51571111) and Jiangsu Province (BK20170645, and BK20201087).

Author contributions

#Y.Q.C. and T.Q.Z. contributed equally in this work. X.R.Z., T.Q.Z. and Y.Q.C. prepared samples and tested the photocatalytical performance. C.L. conducted the SEM test. C.L and Q.R. performed XPS characterization. J.B.F performed TEM test. Y.Q.C. drafted the manuscript. A.D.L. supervised the whole work. W.M.L. and A.D.L. revised the manuscript. All authors critically read and commented on the manuscript. All authors read and approved the final manuscript.

Competing interests

The authors declare no competing interests.

Additional information

Correspondence and requests for materials should be addressed to A.-D.L.

Reprints and permissions information is available at www.nature.com/reprints.

Publisher's note Springer Nature remains neutral with regard to jurisdictional claims in published maps and institutional affiliations.